

RESEARCH ARTICLE

Receptivity of swept-aerofoil flows to small amplitude wall roughness using resolvent analysis based on wall displacement

Euryale Kitzinger¹, Denis Sipp^{1*}, Olivier Marquet¹, and Estelle Piot^{2,1,1}

¹DAAA, ONERA, University of Paris-Saclay, F-92190 Meudon, France

²DMPE, ONERA, University of Toulouse, F-31055 Toulouse, France

*Corresponding author. E-mail: denis.sipp@onera.fr

Received: XX 2020; **Revised:** XX XX 2020; **Accepted:** XX XX 2020

Keywords: Receptivity; Resolvent; Wall roughness; Transition; Cross-flow instability

Abstract

The receptivity of a laminar boundary layer flow to small amplitude wall roughness is investigated on an ONERA-D swept aerofoil by introducing a dedicated resolvent operator based on linearised small amplitude wall displacements. The singular value decomposition of this operator for a given spanwise wavenumber provides optimal wall roughness and flow responses that maximise an input-output gain. At the most receptive spanwise wavenumber, the optimal response is a cross-flow mode associated with an optimal roughness located close to the attachment-line and presenting a wavy shape with a wavevector nearly orthogonal to the external streamlines. The method therefore allows direct identification of the location and structure (chordwise and spanwise wavenumbers) of the most receptive roughness. For various given wall roughness shapes and locations (periodic or compact in the chordwise and/or spanwise directions), an approximation of the response based on the dominant optimal response is shown to accurately match the total response downstream of the roughness. The method therefore allows a straightforward computation of the response of the flow to any given small amplitude roughness.

Impact Statement

The accurate prediction of laminar / turbulent transition on aircraft wings is of major importance for the design of future low-consumption aircraft. Low atmospheric turbulence rates favour transition triggered by unavoidable surface imperfections. Accurate and straightforward prediction of the flow response to a given wall roughness would pave the way to future shape optimisation or control strategies to efficiently delay transition. However, a general method that accounts for all possible instability mechanisms without any approximation (curvature and non-parallelism) is still lacking. This paper describes a new way to determine the properties of the most critical roughness and its associated response, and to calculate, at a reduced cost, the perturbation amplitude triggered by any given low-amplitude wall roughness.

1. Introduction

The laminar or turbulent nature of the boundary layer has a strong impact on aerodynamic aircraft performance. Thus, predicting laminar-turbulent transition and understanding the transitional mechanisms are crucial. The first stage of the laminar-turbulent transition process is receptivity, by which free-stream fluctuations or surface irregularities are transformed into hydrodynamic instabilities within the boundary layer. These perturbations then grow in the streamwise direction taking advantage of the

local instability mechanisms. In the case of swept wings for example, the three main types of instabilities are Attachment-line (AL), cross-flow (CF) and Tollmien-Schlichting (TS) instabilities (Reed & Saric, 1989). Once sufficiently high perturbation amplitudes are reached, nonlinear effects appear. They trigger saturation or new (secondary) instabilities (Herbert, 1988) which may finally lead to transition. When the free-stream perturbations or the surface irregularities are of small amplitude, a linear theory can be used to describe both the initial receptivity process and the first growth phase.

Deyhle & Bippes (1996) have experimentally shown that transverse travelling CF waves are dominant in boundary layers subjected to a high external turbulence rate ($Tu > 0.2\%$), while steady CF waves initiated by surface irregularities dominate for lower turbulence rates, as observed in flight conditions (Carpenter & Reed, 2008) [$Tu = 0.05\%$]. Müller & Bippes (1989) have shown, in the case of a swept flat plate, that steady vortices were triggered by surface irregularities, such as wall roughness. Numerous studies on the receptivity to surface roughness have been carried out during the last decades. Radeztsky & Saric (1999) studied experimentally the influence of wall roughness in the case of a swept wing where the initial stability characteristics are cross-flow dominated. They noticed that transition was triggered most upstream when the roughness was located near the attachment-line. Other experimental studies have been conducted and a review of these works on the influence of surface roughness can be found in Saric & White (2003). From a numerical point of view, Crouch (1993) studied, in a Falkner-Skan-Cooke boundary layer (FSC) within the parallel flow assumption, the competition between receptivity triggered by localised perturbations of the surface geometry and by acoustic waves in the free-stream. He confirmed that at high sweep angle, when considering acoustic waves representative of flight conditions, the boundary layer was dominated by the development of steady cross-flows. Collis & Lele (1999) dealt with the receptivity to spanwise-periodic surface roughness on a swept parabolic cylinder. They showed that surface curvature and, more significantly, non-parallelism plays an important role in receptivity computations. Schrader & Henningson (2009) considered non-parallelism for the study of the receptivity to wall roughness of a three-dimensional boundary layer. They modelled a swept wing leading edge with an FSC-like boundary layer with a favourable pressure gradient. They confirmed that, when the turbulence rate was low, steady CF waves dominated the receptivity process over unsteady CF waves induced by free-stream disturbances. They observed that the receptivity mechanism was fully linear when the height of the roughness was below 5% of the displacement thickness. Comparing the results obtained with a meshed roughness in a DNS and the ones from a parabolised stability equations (PSE) approach with a linear roughness model, Tempelmann *et al.* (2012b) concluded that the linear model was valid up to a roughness height of 0.1 of the displacement thickness.

In boundary layer flow, streamwise energy amplification may also occur due to non-modal (local) effects (even when flows are exponentially spatially stable). Contrary to two-dimensional boundary layers, few studies exist on the non-modal growth of three-dimensional boundary layers. Corbett & Bottaro (2001) have computed, in the case of the FSC within parallel-flow assumption, the perturbations with the largest transient gain over a fixed period of time. They showed that, in contrast to the two-dimensional case, both modal and non-modal growths exhibit similar structures, with the optimal perturbations evolving into vortices almost aligned with the direction of the outer flow, which finally trigger streaks with the lift-up mechanism. These observations were confirmed by Tempelmann *et al.* (2010) who studied the same flow using a spatial framework and PSE allowing them to take into account non-parallel effects.

In order to capture all instability mechanisms (AL, CF, TS, non-modal) and the effects of non-parallelism and surface curvature, global stability analyses (at least in the chordwise direction) on a swept profile were initiated by Tempelmann *et al.* (2012a). They used solutions of the adjoint linearised Navier-Stokes (ALNS) equations to explore the receptivity of cross-flow perturbations on a swept wing of infinite span. They studied in particular the roughness shape leading to the perturbations with the largest amplitude at the domain outflow. It corresponds to a wavy shape in the chordwise direction that is maximal in the vicinity and just downstream of the attachment-line. The method relies on global direct (resp. adjoint) stability computations with an upstream (resp. downstream) Dirichlet boundary condition determined with a local spatial direct (resp. adjoint) stability computation. The computational

domain therefore needs to be chosen in such a way that the same local instability branch be identified at the upstream (direct) and downstream (adjoint) boundaries, which requires some tuning and a precise knowledge of the instability mechanisms. [Thomas & Ashworth \(2017\)](#) used a similar method and a large number of receptivity calculations have been performed for different forcing by computing only once the solutions of the LNS and ALNS equations. In particular, they have confirmed that cross-flow instabilities were more affected by roughness near the attachment-line.

The present paper aims at studying the receptivity to small amplitude wall roughness by introducing a dedicated resolvent analysis ([Trefethen & Driscoll, 1993](#); [Schmid & Henningson, 2001](#)). Its input is a small amplitude wall deformation (instead of a volume forcing) while the output is, as before, the energy of the perturbation integrated over the volume. The modelling of the wall deformation is based on a linear model, the validity of which has been examined notably by [Schrader & Henningson \(2009\)](#); [Tempelmann *et al.* \(2012b\)](#). The singular value decomposition of resolvent operators has been widely used to study the energy amplification due to both modal and non-modal mechanisms in transitional flows ([Sipp & Marquet, 2013](#); [Symon & McKeon, 2018](#)). It allows the consideration of non-modal mechanisms and to take into account non-parallelism in boundary layer or free-shear flows. Compared to the method used by [Thomas & Ashworth \(2017\)](#); [Tempelmann *et al.* \(2012a\)](#), it also has the benefit of not relying on relevant inlet / outlet boundary conditions, that come from local direct and adjoint spatial stability solutions: such a method in particular requires to identify a local spatial modal at the inlet of the computational domain that is connected to a local spatial mode at the outlet of the domain. Hence, only local modal spatial instabilities can be dealt with that method and the inlet and outlet boundaries need to be located in specific regions (for the case considered in the present article, we will even show that it is not possible to follow this mode from the inlet to the outlet of the domain). Note that a PSE-based method instead of local spatial stability analysis could mitigate this problem: yet, this method still needs to be initialised at the inlet by a local spatial mode and it does not handle local non-modal instabilities ([Towne *et al.*, 2019](#)). In contrast, the present resolvent based method does not suffer from these limitations since it is the optimisation process of the input-output dynamics that automatically identifies the most energetic forcings and responses, even in the case of local non-modal instabilities and in the case of strong non-parallelism. Also, the use of the resolvent operator to solve the LNS equations gives access to the response amplitude in the vicinity of the location of the roughness and the use of the singular value decomposition has the advantage of providing two orthonormal bases, one for the input space and one for the output space. When a singular value is strongly dominant, the analysis gives intrinsic information about the physics of the flow by showing the leading instability mechanism, both in response and in forcing. In this case, once few optimal forcings and responses have been computed, the calculation of the response to a given roughness can be approximated by only computing few scalar products, which results in a reduced computational cost compared to the systematic resolution of the LNS equations. Moreover, the prediction of the full response based on the dominant optimal forcings / responses will be accurate downstream of the roughness, which is usually sufficient for laminar / turbulent transition predictions. We will assess the accuracy of the prediction when using the dominant singular value for both periodic and compact roughness in the chordwise and spanwise directions. The method will be illustrated on the swept ONERA-D aerofoil, a configuration that was already studied (base-flow and neutral stability curves of attachment-line, cross-flow and Tollmien-Schlichting perturbations) in [Kitzinger *et al.* \(2023\)](#).

The outline of the paper is the following. In §2, we describe the flow configuration, in §3 the wall displacement based resolvent analysis and the approximations and in §4 the numerical methods. In §5, the results are illustrated for the ONERA-D aerofoil. The properties of the optimal roughness and responses are explored in §5.1 and the perturbations triggered by particular roughness are studied in §5.2. We validate in particular in this last sub-section the low-rank approximation against the exact response (given by the resolvent) for various roughness shapes.

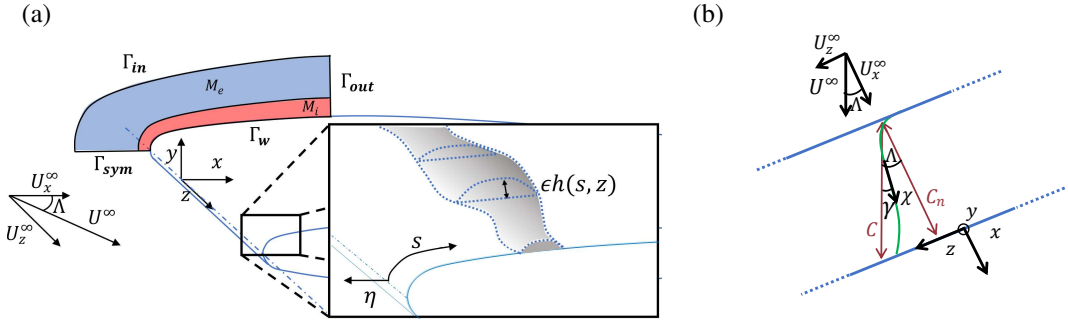


Figure 1. (a): Schematic of the mesh and flow configuration with a zoom on a roughness of any shape. (b): Angles and coordinate systems are indicated. An external streamline is illustrated in green. The blue lines correspond to the leading/trailing edges.

2. Flow configuration

We investigate the incompressible flow around an aerofoil of chord C and of infinite span. The origin of the orthonormal coordinate system (x, y, z) is located at the leading edge of the aerofoil, whose direction is denoted z . As shown in figure 1, the x - and y -directions are orthogonal to the leading edge and to the symmetry plane of the aerofoil, respectively. The uniform upstream velocity is of constant magnitude U^∞ and oriented in a direction defined by the sweep angle Λ and the angle of attack α , that is zero in the present study. The sweep velocity denoted $U_z^\infty = U^\infty \sin \Lambda$ is the component of the upstream velocity in the spanwise direction while the chordwise velocity $U_x^\infty = U^\infty \cos \Lambda$ is the component in the chordwise direction. Note that C denotes the aerofoil's chord in the direction of the upstream velocity while $C_n = C \cos \Lambda$ is the chord normal to the aerofoil's leading edge. In the following, all variables are made non-dimensional using the chord C_n and the velocity U_x^∞ . The incompressible flow is entirely characterised by two non-dimensional parameters: the sweep angle Λ and the Reynolds number $Re_{C_n} = U_x^\infty C_n / \nu$, ν being the kinematic viscosity of the fluid. The local coordinate system (s, η, z) is shown in the close-up view of figure 1(a). s is the curvilinear abscissa along the surface of the profile in the plane orthogonal to the spanwise z -direction and η the local wall normal direction. Thus, $\eta = 0$ corresponds to the aerofoil's wall. The local direction of the streamline of the external baseflow velocity field χ is shown in figure 1(b).

3. Theory

We investigate the incompressible three-dimensional steady flow surrounding a rough aerofoil infinitely long in the spanwise direction z . The non-dimensional flow velocity $U_T(x, y, z)$ and pressure $P_T(x, y, z)$ fields are governed by the steady incompressible Navier-Stokes equations

$$(U_T \cdot \nabla) U_T + \nabla P_T - Re_{C_n}^{-1} \nabla^2 U_T = \mathbf{0}, \quad \nabla \cdot U_T = 0 \text{ in } \Omega_r, \quad U_T = \mathbf{0} \text{ on } \Gamma_r, \quad (1)$$

where the gradient is classically defined as $\nabla = (\partial_x, \partial_y, \partial_z)^T$. The momentum and mass equations are satisfied in the spatial domain Ω_r surrounding the aerofoil and the roughness. The boundary formed by the aerofoil and the roughness is denoted Γ_r , on which a no-slip velocity condition is imposed.

As sketched in the close-up view of figure 1(a), we further assume that the height of any wall roughness, denoted $\epsilon h(s, z)$, is infinitesimally small compared to the thickness / chord of the smooth aerofoil, the surface of the latter being denoted Γ_w . In the local curvilinear coordinate system, the surface

of Γ_r is thus described by $(s, \eta = \epsilon h(s, z), z)$ with $\epsilon \ll 1$, while the surface of the smooth aerofoil Γ_w is $(s, \eta = 0, z)$. The roughness being considered as a small perturbation of the smooth aerofoil geometry, we decompose the flow variables as

$$(\mathbf{U}_T, P_T) = (\mathbf{U}, P) + \epsilon(\mathbf{u}, p),$$

where (\mathbf{U}, P) denotes the flow over the smooth aerofoil while (\mathbf{u}, p) is the flow perturbation induced by the roughness. This decomposition is injected into the governing equations (1) to obtain, at zeroth-order the equations the flow around the smooth aerofoil, and at ϵ order the wall roughness perturbation equations. In particular, the no-slip boundary condition along Γ_r reads

$$\mathbf{0} = \mathbf{U}_T(s, \epsilon h(s, z), z) \approx \mathbf{U}(s, 0, z) + \epsilon [\mathbf{u} + h \partial_\eta \mathbf{U}](s, 0, z) + \dots$$

This Taylor expansion shows that, at first order in ϵ , the small roughness is equivalent to the velocity perturbation over the smooth aerofoil

$$\mathbf{u}(s, 0, z) = -h \partial_\eta \mathbf{U}. \quad (2)$$

The validity of this linearised velocity condition for modelling the effect of a roughness on a boundary layer flow was addressed by (Schrader & Henningson, 2009; Tempelmann *et al.*, 2012b) who found that this is a valid approximation for roughness height below $0.05\delta^*$, δ^* being the displacement thickness of the boundary layer.

3.1. Steady flow over the smooth aerofoil

The equations governing the baseflow velocity field $\mathbf{U}(x, y) = (U, V, W)^T$ around the swept smooth aerofoil are the steady Navier-Stokes equations:

$$(\mathbf{U} \cdot \nabla) \mathbf{U} + \nabla P - Re^{-1} \nabla^2 \mathbf{U} = \mathbf{0}, \quad \nabla \cdot \mathbf{U} = 0 \text{ in } \Omega, \quad \mathbf{U} = \mathbf{0} \text{ on } \Gamma_w. \quad (3)$$

As the aerofoil is symmetric and the angle of attack is zero, the domain Ω may be restricted to the upper half domain, i.e. $y > 0$. A symmetric boundary condition $(\partial_y U_x, U_y, \partial_y U_z) = (0, 0, 0)$ is applied at the symmetric boundary $\Gamma_{sym} = \{x < 0, y = 0\}$. As shown in figure 1(a), the spatial domain Ω does not extend up to the trailing-edge of the aerofoil. To specify the boundary conditions at the inflow Γ_{in} and outflow Γ_{out} boundaries of this domain, we first determine the symmetric potential velocity field $(U_x^p, U_y^p, U_z^p) = (\partial_y \psi, -\partial_x \psi, U_z^\infty = \tan(\Lambda))$ with the stream-function ψ satisfying the Laplace equation $\Delta \psi = 0$, in a sufficiently large domain Ω_p so that we may impose the uniform velocity condition $\psi = y$ on the far-field boundary Γ_p . On Γ_w and Γ_{sym} , we set $\psi = 0$, which allows the smooth aerofoil to be a streamline and the flow field to be symmetric. This potential velocity is then imposed as a Dirichlet boundary condition at the inlet boundary Γ_{in} of the domain Ω , i.e.

$$(U_x, U_y, U_z) = (U_x^p, U_y^p, U_z^\infty) \text{ on } \Gamma_{in}, \quad (4)$$

while the pressure field of the potential flow $P^p = [1 - (U_x^p)^2 - (U_y^p)^2]/2$ and a Neumann condition for the velocity field are applied at the outlet:

$$\partial_x \mathbf{U} = \mathbf{0} \text{ and } P = P^p \text{ on } \Gamma_{out}. \quad (5)$$

3.2. Wall-displacement induced perturbation

We consider a roughness that may be harmonic, periodic or compact in either the curvilinear s - or span-wise z -directions. The linear equations governing the three-dimensional flow perturbation $(\mathbf{u}, p)(x, y, z)$

induced by this roughness are:

$$(\mathbf{u} \cdot \nabla) \mathbf{U} + (\mathbf{U} \cdot \nabla) \mathbf{u} + \nabla p - Re_{C_n}^{-1} \nabla^2 \mathbf{u} = \mathbf{0}, \quad \nabla \cdot \mathbf{u} = 0 \text{ in } \Omega \quad \mathbf{u} = -h \partial_\eta \mathbf{U} \text{ on } \Gamma_w. \quad (6)$$

As explained before, the presence of the roughness over the smooth aerofoil is accounted for with the linearised wall boundary condition. The solution of the above linear problem with non-homogeneous boundary conditions at the wall is the sum of the solution of the problem with homogeneous condition and a particular forced solution. We choose the Reynolds number and sweep angle so as to have a globally stable base-flow, so that all homogeneous solutions tend to zero at large times. We hence only consider the forced response. Interestingly, the spanwise-dependency of the flow perturbation is only due to the spanwise dependency of the roughness $h(s, z)$, since the velocity \mathbf{U} is invariant in the spanwise direction. Hence, any roughness and triggered perturbation can be further decomposed into Fourier modes as

$$h(s, z) = \int_{-\infty}^{\infty} \hat{h}_\beta(s) e^{i\beta z} d\beta, \quad \mathbf{u}(x, y, z) = \int_{-\infty}^{\infty} \hat{\mathbf{u}}_\beta(x, y) e^{i\beta z} d\beta \quad (7)$$

where β is the (real) spanwise wavenumber and the corresponding (complex) Fourier modes of the wall roughness and flow response are denoted $\hat{h}_\beta(s)$ and $\hat{\mathbf{u}}_\beta(x, y)$, respectively. Note that the case of periodic roughness in z may be handled by stating that $\hat{h}_\beta(s) = \sum_m \delta(\beta - m\beta_0) \hat{h}_{m\beta_0}(s)$ with $\beta_0 = 2\pi/L_z$ being the fundamental wavenumber in z and $\delta(\beta)$ the Dirac function at $\beta = 0$. Since the three-dimensional roughness $h(s, z)$ and flow perturbation $\mathbf{u}(x, y, z)$ are real quantities, the corresponding complex Fourier modes satisfy $\hat{h}_{-\beta} = \overline{\hat{h}_\beta}$ and $\hat{\mathbf{u}}_{-\beta} = \overline{\hat{\mathbf{u}}_\beta}$ where $\overline{(\cdot)}$ denotes the complex conjugate.

Injecting this Fourier decomposition into (6), we obtain

$$\begin{cases} (\hat{\mathbf{u}}_\beta \cdot \nabla) \mathbf{U} + (\mathbf{U} \cdot \nabla_\beta) \hat{\mathbf{u}}_\beta + \nabla_\beta \hat{p}_\beta - Re_{C_n}^{-1} \nabla_\beta^2 \hat{\mathbf{u}}_\beta = \mathbf{0}, & \nabla_\beta \cdot \hat{\mathbf{u}}_\beta = 0 \text{ in } \Omega \Rightarrow \mathcal{L}_\beta \cdot (\hat{\mathbf{u}}_\beta, \hat{p}_\beta)^T = \mathbf{0} \text{ in } \Omega, \\ \hat{\mathbf{u}}_\beta = -\hat{h}_\beta \partial_\eta \mathbf{U} \text{ on } \Gamma_w \Rightarrow \hat{\mathbf{u}}_\beta = \mathcal{F} \hat{h}_\beta \text{ on } \Gamma_w, \end{cases} \quad (8)$$

where the gradient and Laplacian operators applied on the Fourier modes are defined as $\nabla_\beta = (\partial_x, \partial_y, i\beta)^T$. \mathcal{L}_β is the linearised Navier-Stokes operator and \mathcal{F} is the operator that transforms the wall normal displacement \hat{h}_β into a velocity $\hat{\mathbf{u}}_\beta$ with appropriate Dirichlet boundary conditions on the wall and zeros inside the domain. The boundary conditions at the inflow and outflow boundaries are $\hat{\mathbf{u}}_\beta = \mathbf{0}$ on Γ_{in} and $\hat{p}_\beta \mathbf{e}_x - Re_{C_n}^{-1} \partial_x \hat{\mathbf{u}}_\beta = 0$ on Γ_{out} and we restrict our analysis to symmetric perturbations, i.e. $(\partial_y \hat{u}_{\beta,x}, \hat{u}_{\beta,y}, \partial_y \hat{u}_{\beta,z}) = (0, 0, 0)$ on Γ_{sym} . We can thus calculate the flow perturbation triggered by a roughness over the smooth aerofoil without modifying the geometry, by using the steady flow \mathbf{U} over the smooth aerofoil and by applying the linearised wall velocity condition at its surface. After spatial discretisation, the equations (8) with the above boundary conditions can be recast in an input-output form:

$$\hat{\mathbf{u}}_\beta = R_\beta \hat{h}_\beta, \quad (9)$$

where $R_\beta = P^* L_\beta^{-1} P F$. The matrices L_β and F are respectively the discrete form of the continuous operators \mathcal{L}_β and \mathcal{F} defined in equations (8). The matrix P designates the prolongation operator which adds a zero pressure component to a given velocity vector.

\hat{h}_β denotes the discrete vector of the function $\hat{h}_\beta(s)$, and $\hat{\mathbf{u}}_\beta$ is the discrete velocity vector of the continuous vectorial field $\hat{\mathbf{u}}_\beta(x, y)$. In the following, the spatial coordinates (x, y) are specified to distinguish the continuous and discrete forms of the velocity vector. R_β will be called the "resolvent" matrix (even though it is not a square matrix) and can be considered as a transfer function taking a wall roughness Fourier mode \hat{h}_β as input and giving the flow-perturbation Fourier mode $\hat{\mathbf{u}}_\beta$ as output.

3.3. Resolvent analysis with wall displacements

We will now determine two orthonormal bases, one for the (input) wall roughness Fourier modes and one for the (output) flow-response Fourier modes. For this, we define the kinetic energy of the triggered perturbation $\langle \hat{\mathbf{u}}_\beta(x, y), \hat{\mathbf{u}}_\beta(x, y) \rangle = \int_\Omega \hat{\mathbf{u}}_\beta^*(x, y) \hat{\mathbf{u}}_\beta(x, y) dx dy$ in the domain Ω as a measure of the output space, where $(\cdot)^*$ refers to the transconjugate and $\langle \hat{h}_\beta(s), \hat{h}_\beta(s) \rangle_w = \int_{\Gamma_w} \overline{\hat{h}_\beta(s)} \hat{h}_\beta(s) ds$ as a measure of the input space. The discrete form for each measure is then denoted $\hat{\mathbf{u}}_\beta^* Q_u \hat{\mathbf{u}}_\beta$ and $\hat{\mathbf{h}}_\beta^* Q_h \hat{\mathbf{h}}_\beta$, respectively. Then, we introduce the energetic gain G_β to be maximised as the ratio between the output and input measures, i.e.

$$G_\beta = \frac{\hat{\mathbf{u}}_\beta^* Q_u \hat{\mathbf{u}}_\beta}{\hat{\mathbf{h}}_\beta^* Q_h \hat{\mathbf{h}}_\beta} = \frac{\hat{\mathbf{h}}_\beta^* R_\beta^* Q_u R_\beta \hat{\mathbf{h}}_\beta}{\hat{\mathbf{h}}_\beta^* Q_h \hat{\mathbf{h}}_\beta}, \quad (10)$$

where the input-output relation (9) has been used in the numerator. The solution of the optimisation problem $\max_{\hat{\mathbf{h}}_\beta} G_\beta$ and the optimal roughness / responses are finally obtained by solving the two problems:

$$R_\beta^* Q_u R_\beta \hat{\mathbf{h}}_{\beta,j} = \sigma_{\beta,j}^2 Q_h \hat{\mathbf{h}}_{\beta,j}, \quad \hat{\mathbf{u}}_{\beta,j} = \sigma_{\beta,j}^{-1} R_\beta \hat{\mathbf{h}}_{\beta,j}. \quad (11)$$

The optimal roughness $\hat{\mathbf{h}}_{\beta,j}$ and optimal flow responses are normalised as $\langle \hat{h}_{\beta,j}(s), \hat{h}_{\beta,j}(s) \rangle_w = 1$ and $\langle \hat{\mathbf{u}}_{\beta,j}(x, y), \hat{\mathbf{u}}_{\beta,j}(x, y) \rangle = 1$. Note that a fully continuous framework for the definition of these quantities also exists but is not shown here for conciseness. The set of eigenvectors $(\hat{h}_{\beta,j}(s))_{j \geq 1}$ form an orthonormal basis of the forcing space with respect to $\langle \cdot, \cdot \rangle_w$, while the optimal responses $(\hat{\mathbf{u}}_{\beta,j}(x, y))_{j \geq 1}$ constitute an orthonormal basis of the response space with respect to $\langle \cdot, \cdot \rangle$. In our study, we sort the singular values such that $\sigma_{\beta,1} \geq \sigma_{\beta,2} \geq \sigma_{\beta,3} \geq \dots$ so that the optimal forcing $\hat{h}_{\beta,1}(s)$ is related to $\sigma_{\beta,1}^2 = \max_{\hat{\mathbf{h}}} G_\beta$.

We can now compute the response $\hat{\mathbf{u}}_\beta(x, y)$ in equation (9) using the resolvent mode bases:

$$\hat{\mathbf{u}}_\beta(x, y) = \sum_{j \geq 1} \sigma_{\beta,j} \gamma_{\beta,j} \hat{\mathbf{u}}_{\beta,j}(x, y), \quad (12)$$

with $\gamma_{\beta,j} = \langle \hat{h}_{\beta,j}(s), \hat{h}_\beta(s) \rangle_w$ the projection coefficients of the wall roughness Fourier mode $\hat{h}_\beta(s)$ onto the resolvent modes $\hat{h}_{\beta,j}(s)$. In the case where the first singular value is much larger than the following ones, which is generically the case when an instability mechanism is at play, we can neglect the contribution of the next terms: if $\sigma_{\beta,1} |\gamma_{\beta,1}| \gg \sigma_{\beta,j} |\gamma_{\beta,j}| \quad \forall j \geq 2$, we can consider only the contribution of the dominant optimal response: $\hat{\mathbf{u}}_\beta(x, y) \approx \sigma_{\beta,1} \gamma_{\beta,1} \hat{\mathbf{u}}_{\beta,1}(x, y)$.

We then obtain an approximation of the response $\mathbf{u}(x, y, z)$ triggered by the roughness $h(s, z)$ following

$$\mathbf{u}(x, y, z) \approx \int_{-\infty}^{+\infty} \sigma_{\beta,1} \gamma_{\beta,1} \hat{\mathbf{u}}_{\beta,1}(x, y) e^{i\beta z} d\beta, \quad (13)$$

and the local perturbation energy averaged over the spanwise direction reads:

$$\langle \|\mathbf{u}\|^2 \rangle_z(x, y) = \int_{-\infty}^{+\infty} \sigma_{\beta,1}^2 |\gamma_{\beta,1}|^2 \|\hat{\mathbf{u}}_{\beta,1}\|^2(x, y) d\beta, \quad (14)$$

where $\langle \cdot \rangle_z = \lim_{L_z \rightarrow \infty} (1/L_z) \int_0^{L_z} (\cdot) dz$. Explicit approximations may then be obtained by evaluating the integral with a fourth order extended Simpson's rule (Press *et al.*, 2007) over a finite wavenumber range, as discussed in section 5.2.2.

4. Numerical methods

All numerical aspects are handled with FreeFEM (Hecht, 2012), an open-source partial-differential-equations solver that allows to implement spatial discretisation with the Finite Element method. Solutions of resulting large-scale linear problems are computed on multiple processors using the FreeFEM's interface with the Portable, Extensible Toolkit for Scientific Computation (PETSc) (Balay *et al.*, 2022). The interface with the SLEPc solver (Hernandez & Vidal, 2005) is used to compute the solution of eigenvalue problems. We refer to Moulin *et al.* (2019) for didactic examples of these two interfaces in the context of linear stability analysis of large-scale hydrodynamic eigenvalue problems. Taylor-Hood finite elements are used for the spatial discretisation of non-linear base-flow equations (3) and linear perturbation equations (8). The velocity and pressure fields are respectively expanded on second-order (P_2) and first-order (P_1) Lagrange finite elements. A Streamline-Upwind Petrov–Galerkin (SUPG) method together with grad–div stabilisation (Ahmed & Rubino, 2019) is used to compute the base-flow solution while no SUPG stabilisation is considered for the perturbation. A Newton-Raphson method is implemented in FreeFEM to compute solutions of the nonlinear base-flow equations (3), using the potential flow solution as initial condition of this iterative algorithm. The direct sparse LU-solver MUMPS (Amestoy *et al.*, 2001, 2019) is called within PETSc to compute the solution of linear problems at each iteration of the algorithm. For the resolvent analysis, a Krylov-Schur algorithm is used to compute the largest eigenvalues of the eigenproblem (11). The application of the matrices R_β and R_β^* to input vectors provided by the Krylov-Schur algorithm requires the solution of linear problems that are obtained with the MUMPS solver, again.

As shown in figure 1, we consider a two-dimensional domain Ω covering the upper half of the aerofoil and which extends up to 15% in the chordwise x -direction. Two different body-fitted meshes are used to compute the base-flow and resolvent analysis. For the base-flow solution, this mesh is composed of 120000 triangles. It is made up of an internal M_i part (red in figure 1, 100000 triangles) and an external M_e part (blue, 20000 triangles). For the resolvent analysis, we use only the internal mesh M_i , the boundary Γ_{in} being sufficiently far from the profile so that 0-Dirichlet boundary conditions may be imposed. For more details, we refer to Kitzinger *et al.* (2023) where the same mesh was used to perform global stability analysis of the baseflow solution. In particular, the effect of the chordwise extension of the domain and of grid refinement was assessed for the computation of base-flows and neutral curves (marginal eigenvalues of the Jacobian L_β). A similar convergence study (not reported here) was performed for the singular values and resolvent modes to insure that reported results are robust to spatial discretisation.

5. Results

In the present study, we consider the parameters $Re_{C_n} = 1.39 \times 10^6$, $\Lambda = 65.8^\circ$, which corresponds to a globally stable flow for all spanwise wavenumbers (Kitzinger *et al.*, 2023) and thus allows the input-output analysis described in §3.3. In that study, the Reynolds number and sweep angle were chosen to allow the computation of the neutral curve associated to the various instabilities, which remains simple only at high sweep angles. Yet, for the present study, which relies on the more robust resolvent analysis to characterise the instabilities, lower sweep angles could have been chosen. We decided to keep the initial parameters to focus the paper on the novelty, which is methodological. Hence, extensive discussions about the base-flow solution can be found in Kitzinger *et al.* (2023). We recall that it was validated by comparing the external streamline velocity component and the cross-flow component within the boundary layer with those obtained by using an ONERA in-house boundary layer code which solves the Prandtl's equations (Houdeville, 1992). We observed a close agreement between the results obtained with both methods.

For the description of the results, the spanwise wavenumber β of the perturbations will be scaled with Δ which is a measure of the boundary layer thickness at the attachment-line based on the potential flow (Mack & Schmid, 2011). It is defined as $\Delta = \partial U_s^P / \partial s|_{x=0, y=0}$, where U_s^P denotes the s -component of

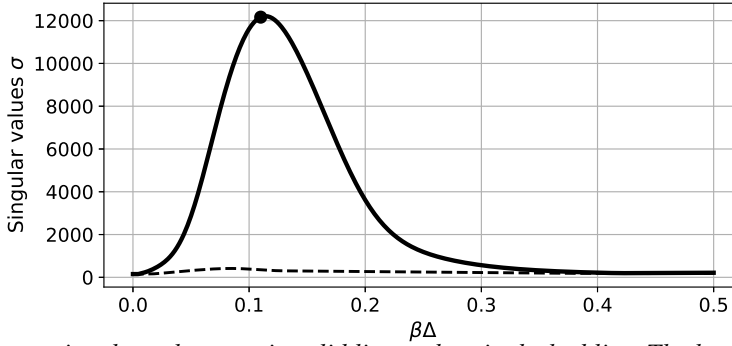


Figure 2. First two singular values: σ_1 in solid line and σ_2 in dashed line. The largest singular value ($\beta\Delta = 0.11$) is marked with a circle.

the potential flow solution. In [Kitzinger et al. \(2023\)](#), it was shown that this thickness corresponds to the displacement thickness at the attachment-line. For the present configuration, we have $\Delta = 9.71 \times 10^{-5}$.

5.1. Wall-displacement resolvent modes

Figure 2 shows the first two singular values σ_1 and σ_2 as a function of the spanwise wavenumber $0 \leq \beta\Delta \leq 0.5$. For values of $\beta\Delta$ between 0.05 and 0.2, the first singular value is significantly higher than the second one, making the resolvent operator be close to rank 1. The second singular value has a maximum of $\sigma_2 = 415$ reached for $\beta\Delta = 0.08$, while the maximum of the first singular value is achieved for $\beta\Delta = 0.11$ where $\sigma_1 = 12162$. The singular value σ_1 for $\beta\Delta = 0.11$, highlighted by the black circle, corresponds to the configuration that is studied in more detail in the following.

5.1.1. Optimal roughness and response for $\beta\Delta = 0.11$

We now analyse the spatial structure of the optimal response and roughness for the spanwise wavenumber close to the largest singular value, i.e. $\beta\Delta = 0.11$. In figure 3 are represented the iso-surfaces of the real part of the optimal roughness and of the spanwise velocity of the optimal response. The optimal roughness is located at the beginning of the leading edge and is oriented in a direction close to the external streamline. The optimal response has a large magnitude on the whole leading edge except at the attachment-line. It consists in steady vortices whose axes are nearly parallel to the external streamlines.

To help discern the type of instability, as commonly done in local stability approaches ([Arnal & Casalis, 2000](#)), we introduce the Ψ angle between the local planar wave vector $\vec{k}(s) = [k_s(s), k_z]$ of the mode and the local direction of the external baseflow streamline: $\Psi = \text{angle}(\vec{k}(s), \vec{U}^e(s))$. Such a planar wave-vector may be approximated as follows: if $\hat{u}(x, y)e^{i\beta z}$ is a component of the perturbation, then $(k_s, k_z) = (\partial_s \phi, \beta)$ where $\phi(s, \eta) = \arg \hat{u}(s, \eta)$. The choice of the component and wall normal distance η does not matter as long as the flow is weakly non-parallel (condition for the existence of such a local wave-vector). Here we used the \hat{u}_y -component and $\eta = \delta_{99}/2$ where δ_{99} is the wall normal distance such as $U_\chi(\delta_{99}) = 0.99U_\chi^e$. The same technique may be used to obtain a Ψ angle for the optimal roughness $\hat{h}(s)e^{i\beta z}$.

The magnitude and orientation of the optimal roughness as well as of the associated perturbation are displayed in figure 4 and the pressure gradient.

The real part of the optimal roughness is plotted in figure 4(a). Its amplitude is close to zero at both extremities of the domain and reaches its maximum magnitude at $s \approx 0.008$. It also has a second (weaker) local maximum at $s = 0.05$ with a second amplification region starting at $s = 0.04$. The curvilinear evolution of the Ψ angle of the optimal roughness is represented in red in figure 4(c). We observe that it remains close to 90° on the whole domain, with small variations up to $s = 0.04$.

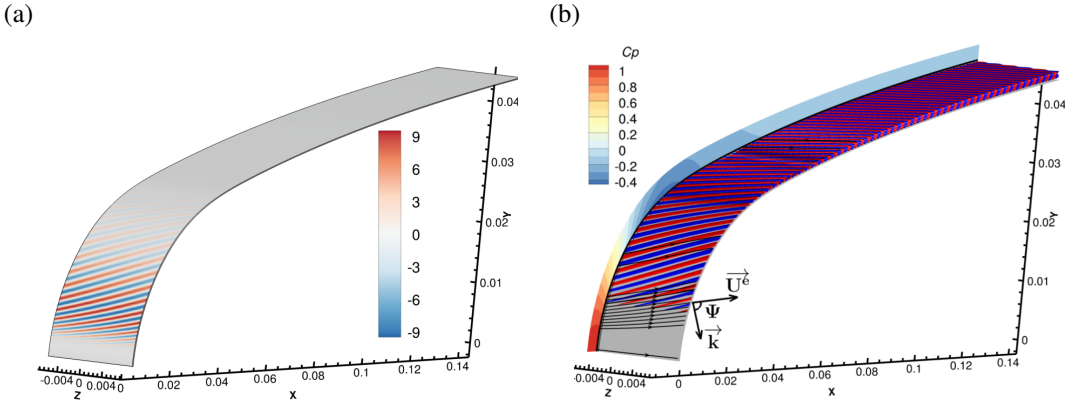


Figure 3. Spatial structure of the real part of: the optimal roughness $\Re(\hat{h}_{0.11/\Delta,1}(s)e^{i\beta z})$ (a) and the z -velocity of the response $\Re(\hat{u}_{0.11/\Delta,1,z}(x,y)e^{i\beta z})$ (b). 2 iso-surfaces at ± 0.1 times the absolute maximum are represented in red and blue. Pressure coefficient C_p , boundary layer thickness δ_{99} (black line), and potential streamlines (black arrow lines) are shown. An example of wavevector and Ψ angle is also displayed.

Concerning the optimal perturbation, the magnitude of the mode as a function of s is plotted in figure 4(d). The magnitude $d_{\hat{u}}(s)$ is defined as $d_{\hat{u}}(s) = \sqrt{\int_0^{L_\eta} \|\hat{u}(s,\eta)\|^2 d\eta}$, where $L_\eta = 45\Delta$. We notice a weak magnitude at $s = 0$, a strong amplification from $s = 0$ to $s = 0.01$, a decrease around $s = 0.05$ and finally a second amplification from $s = 0.057$ up to $s = 0.1$. The evolution according to s of its Ψ angle is displayed in blue in figure 4(c) and we also notice a value close to 90° on the whole domain. Figure 4(b) represents, as a function of s , the pressure gradient scaled using $U_\tau = (\nu\partial_\eta U_\chi(\eta = 0))^{0.5}$ and ν . In the ONERA-D case, the streamwise pressure gradient is negative up to $s = 0.035$, then positive until the limit of the domain, with a flattening around $s = 0.09$. This pressure-gradient changeover is typical of a flow on a swept wing and leads to the existence of two inflection points in the crossflow velocity profile for some values of s (Wassermann & Kloker, 2005; Arnal & Casalis, 2000). A negative pressure gradient is favourable to the development of crossflow waves, which accounts for the increase in the magnitude of the response at the beginning of the domain, while a positive pressure gradient is generally responsible for the growth of Tollmien-Schlichting waves. Additional results about the baseflow for a configuration close the current one are presented in Kitzinger *et al.* (2023).

Based on the characteristics of the optimal response, namely a high magnitude at the leading edge but not in the close vicinity of the attachment-line and a Ψ angle close to 90° , we can conclude that the optimal response is a cross-flow type mode. This is consistent with previous observations of the modes appearing in the case of swept wings with wall roughness (Saric & White, 2003). Moreover, the fact that, having an identical spanwise wavenumber, the optimal roughness and the associated perturbation have an almost equal curvilinear evolution of the Ψ angle shows that they also have a very close evolution of their curvilinear wavenumber $k_s(s)$, as observed by Tempelmann *et al.* (2012a).

A direct link between the double amplification of the optimal roughness and the associated response was not identified. Indeed, when calculating the response associated with a roughness height equal to the optimal roughness height for $s < 0.04$ and to 0 beyond, the same second amplification was observed. This is also shown by the roughness studied in section 5.2.1.

We now compare the magnitude and the Ψ angle of the optimal response with the results obtained using a local stability analysis (figure 4(c, d)). The local stability analysis considers eigenmodes sought in the (s, η, z) reference frame under the form $q = \hat{q}(\eta)e^{i(as+\beta z-\omega t)}$. The spatial stability analysis in the s -direction is solved for fixed β and ω real values. The local stability code solves the one-dimensional differential eigenvalue problem with a high-order scheme. The parallel flow assumption is used, and the

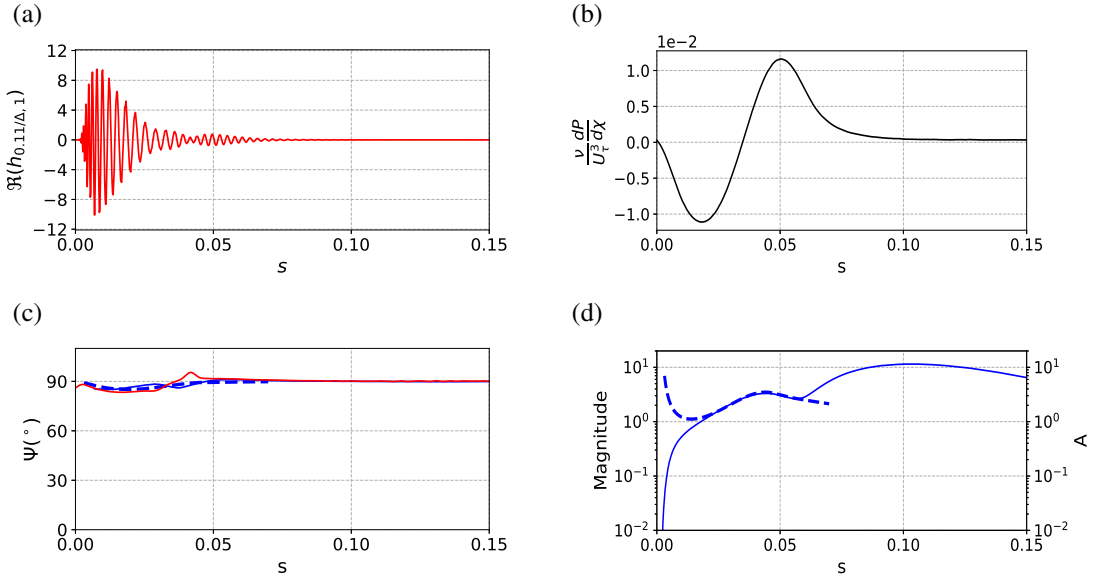


Figure 4. Curvilinear evolution of (a): the optimal roughness. (b): the streamwise pressure gradient made non-dimensional with friction velocity $U_\tau = (\nu \partial_\eta U_\chi(\eta = 0))^{0.5}$ and kinematic viscosity ν . (c): the Ψ angle of the optimal roughness (red) and response (blue). (d): the magnitude of the optimal response. The optimal perturbation obtained with the global resolvent (in solid line) and the mode calculated by a local stability analysis (in dashed line) are represented.

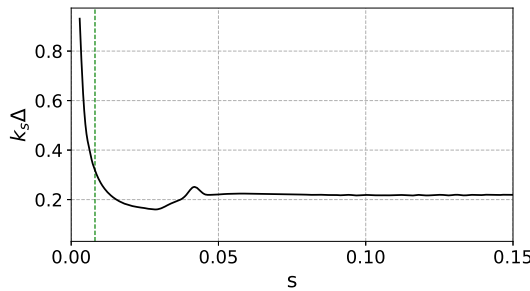


Figure 5. Curvilinear evolution of $k_s \Delta$ of the optimal roughness with $\beta \Delta = 0.11$. The location of the maximum magnitude of the optimal roughness is shown (green vertical dashed line).

flow computed by the boundary-layer solver is used as the baseflow, to avoid interpolation errors from the FEM mesh. In the local stability analysis framework, the Ψ angle is directly derived from the real parts of α and β and the knowledge of the inviscid streamwise direction at each chordwise location. The spatial amplification $A(s)$ is represented in figure 4(d) and is defined as $\ln(A(s)/A_0) = \int_{s_0}^s -\Im(\alpha(s)) ds$ (see for instance Arnal & Casalis, 2000; Reed *et al.*, 1996, for reviews on local stability approach) with the initialisation at $s_0 = 0.003$ and A_0 arbitrarily chosen such as $A(s)$ fits the magnitude of the optimal response. We observe that the Ψ angle and the amplification for $0.018 < s < 0.056$ match very well. For $s < 0.013$, the mismatch is due to the fact that the optimal response is triggered by a roughness, which is not taken into account in the spatial stability analysis. The position of the beginning of the growth phase is the position of branch I and coincides closely with the maximum magnitude of the associated roughness ($s = 0.008$). This is in good agreement with the literature (Tempelmann *et al.*,

2012a; Sipp & Marquet, 2013; Choudhari, 1994). Finally, the second amplification of the mode from the resolvent analysis ($s > 0.057$) could not be captured by the local stability analysis. This may be due to several reasons. First, the second amplification may be caused by a non-modal spatial growth, which is not captured by examining only the most unstable mode of the local stability analysis. Secondly, the assumptions of flow parallelism and no surface curvature used in the local stability analysis are also limiting and may account for this deviation. It is not obvious whether a PSE method, which takes into account weak non-parallelism but does not capture non-modal mechanisms (Towne *et al.*, 2019), would be able to recover this second amplification.

The evolution of the curvilinear wavenumber k_s with respect to s is represented in figure 5 and the position of the maximum magnitude of the optimal roughness is indicated with a green vertical dashed line. The wavenumber k_s decreases from the attachment-line till $s = 0.03$ where $k_s\Delta = 0.16$. At the location of maximum magnitude $s = 0.008$, we get $k_s\Delta = 0.32$. Afterwards, it reaches a local maximum of $k_s\Delta = 0.25$ where the second amplification region begins and is then about 0.22 up to the end of the domain. Moreover, since the spanwise wavenumber is fixed and $\Psi \approx 90^\circ$ on the whole domain, the curvilinear evolution of k_s is closely related to the orientation of the external streamlines.

5.1.2. Optimal roughness and perturbations for $0.05 \leq \beta\Delta \leq 0.3$

The optimal roughness for $\beta\Delta \in [0.05, 0.3]$ have qualitatively similar spatial structures as the one at $\beta\Delta = 0.11$ with two magnitude maxima and zero values at the extremities of the domain as well as a curvilinear wavenumber which varies with s .

In figure 6(a) are plotted according to $\beta\Delta$ the positions of the maximum magnitude of the optimal roughness and perturbation for the different spanwise wavenumbers. Concerning the optimal roughness, the position of the maximum tends to get further away when increasing $\beta\Delta$, moving from $s \approx 0.006$ to $s \approx 0.016$. For all spanwise wavenumber values, the optimal roughness is located relatively close to the attachment-line, thus corroborating the conclusions of previous studies (Radeztsky & Saric, 1999; Thomas & Ashworth, 2017). Contrary to the optimal roughness, the position of the maximum magnitude of the optimal response tends to get closer to the attachment-line with the increase of the spanwise wavenumber, moving from $s = 0.13$ for $\beta\Delta = 0.05$ to $s = 0.022$ for $\beta\Delta = 0.30$.

In figure 6(b) are represented the Ψ angles of the optimal roughness and response at the curvilinear location of the maximum magnitude as a function of $\beta\Delta$. We note that the Ψ angle remains almost constant with the evolution of the spanwise wavenumber with values close to 90° .

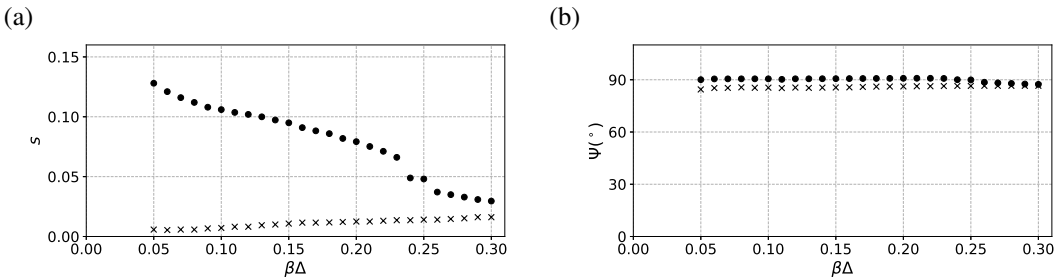


Figure 6. (a): Curvilinear position of the maximum magnitude of the optimal roughness and response as a function of $\beta\Delta$. (b): Local Ψ angle of the optimal roughness and response at the location of the maximum magnitude. The values related to the optimal roughness and responses are respectively depicted by crosses and circles.

These observations on the position of the maximum of the magnitude of the optimal response as well as on the value of the associated Ψ angle tend to show that the optimal response is of cross-flow type for $\beta\Delta \in [0.05, 0.3]$.

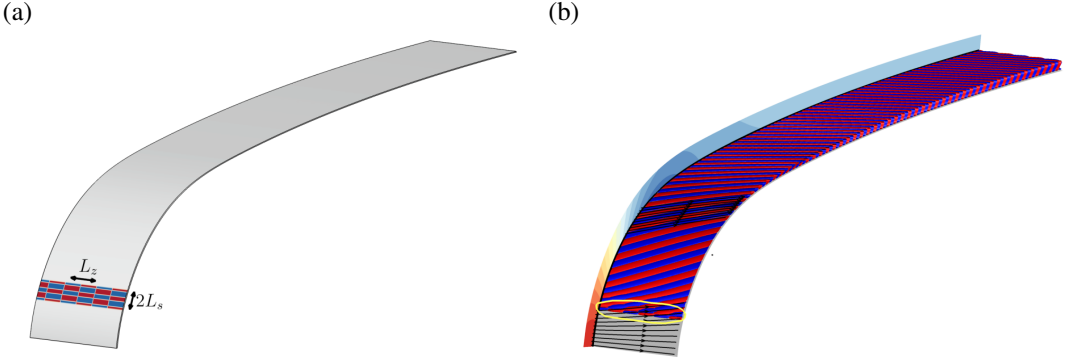


Figure 7. (a): Shape $h(s, z)/H$ of the square wave roughness with $L_z/\Delta = 2\pi/0.11 \approx 57.1$ and $L_s/\Delta = 2\pi/0.32 \approx 19.6$ and localised at $s_0 = 0.008$. The positive and negative values are represented in red and blue, respectively. (b): Associated response calculated solving the LNSE with the same representation as 3. The yellow ellipse indicates the area where a difference with the response calculated using the approximation (18) occurs.

5.2. Flow response to specific roughness

In the present section, we assess the performance of the formulation (12) associated with the approximation (13) to reconstruct the response triggered by localised and non-localised roughness.

5.2.1. Case of square wave roughness localised in the curvilinear s -direction and harmonic in the spanwise z -direction

We consider a roughness periodic (characteristic size $L_z = 2\pi/\beta_0$) in z and which is compact (characteristic size L_s) and localised in the curvilinear direction (around s_0):

$$\frac{h(s, z)}{H} = \frac{1}{2} h_s \left(\frac{s - s_0}{L_s} \right) h_z \left(\frac{z}{L_z} \right), \quad (15)$$

where

$$h_s = -\mathcal{H}_{-1} + 2\mathcal{H}_{-3/4} - 2\mathcal{H}_{-1/4} + 2\mathcal{H}_{1/4} - 2\mathcal{H}_{3/4} + \mathcal{H}_1 \quad (16)$$

$$h_z = -1 + 2\mathcal{H}_0 \text{ for } z \in [-1/2; 1/2[\quad \text{and} \quad h_z(z+1) = h_z(z) \quad \forall z, \quad (17)$$

function \mathcal{H}_ξ referring to the Heaviside function with the discontinuity at ξ . The roughness exhibits a square wave shape of peak-valley distance H , zero mean, both in the chordwise direction s and the spanwise direction z . Its spanwise wavenumber β_0 is chosen so as to coincide with the most amplified spanwise wavenumber optimal roughness ($\beta_0\Delta = 0.11$). We picked L_s close to the local wavelength $L_s = 2\pi/k_s = 2\pi\Delta/(k_s\Delta = 0.32)$ of this optimal roughness at its maximum magnitude occurring at $s_0 = 0.008$ (see figure 5). The roughness centred at $s_0 = 0.008 \approx 82\Delta$ is represented in figure 7. In the following, we will also consider this same roughness but moved around $s_0 = 0.016 \approx 165\Delta$ and $s_0 = 0.056 \approx 577\Delta$: since we keep the same L_s , these roughness are not anymore optimal with respect to the local optimal roughness wavenumber, which is respectively $k_s\Delta = 0.19$ and $k_s\Delta = 0.22$ at these new locations.

Equation (7) for the wall roughness becomes $h(s, z) = (H/2)h_s((s - s_0)/L_s) \sum_{m=-\infty}^{+\infty} \hat{h}_{z,m} e^{im\beta_0 z}$, where $\hat{h}_{z,m}$ is the Fourier transform of a zero-mean square wave, so that $\hat{h}_{z,0} = 0$ and $|\hat{h}_{z,m}| \sim m^{-1}$. Considering an approximation with the dominant singular value and 4 harmonics, equation (12) for the

response provides the following explicit form of the flow response:

$$\frac{\mathbf{u}(x, y, z)}{H} \approx \sum_{m=1}^4 \Re \left(\hat{h}_{z,m} \sigma_{1,m} \left\langle \hat{h}_{1,m}(s), h_s \left(\frac{s-s_0}{L_s} \right) \right\rangle_w \hat{\mathbf{u}}_{1,m}(x, y) e^{im\beta_0 z} \right). \quad (18)$$

The local mean fluctuation rate $\langle \|\mathbf{u}\| \rangle_z(s, \eta)/H$ of the perturbation may then be obtained by an average of the kinetic energy in the spanwise direction, see equation (14).

We have considered three locations of the roughness in figure 8: $s_0 = 0.008$ (blue), $s_0 = 0.016$ (red) and $s_0 = 0.056$ (green). They are represented in figure (a) along with the optimal roughness (black). In figure (b) are represented the curvilinear evolution of the maximum mean fluctuation rate $\max_{\eta} \sqrt{\langle \|\mathbf{u}\|^2 \rangle_z} / H$ of the response obtained by solving the exact equation (9) (dashed lines) and by using the approximation formula defined in (18) (solid lines). A good agreement between the responses is found downstream of the roughness. Hence, if the roughness is sufficiently small not to trigger transition in its vicinity (natural transition), the downstream evolution of the fluctuation rate is well captured by few singular values/harmonics. The magnitude peak at the location of the roughness is more noticeable when the response has low energy, so that the maximum magnitude of the most critical roughness is still well captured by the low-rank approximation (18).

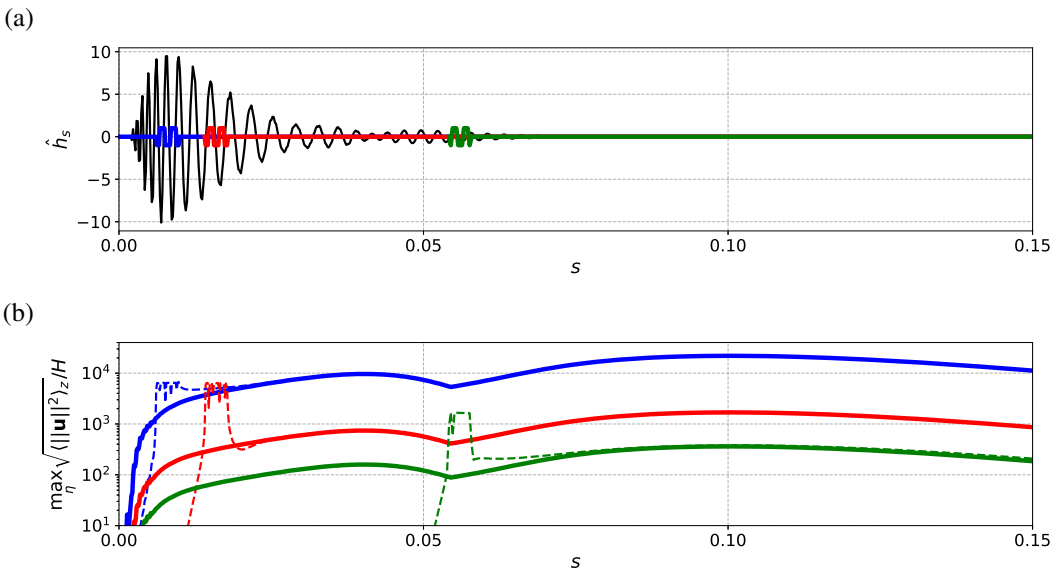


Figure 8. (a): Representation of the optimal roughness (black) and the shape of the square wave roughness $h_s((s-s_0)/L_s)$ localised at $s_0 = 0.008$ (blue), $s_0 = 0.016$ (red) and $s_0 = 0.056$ (green) and $L_s/\Delta \approx 18.5$. The square wave roughness in (a) have been magnified by a factor 2 for visualisation purposes. (b): Curvilinear evolution of the maximum mean fluctuation rate $\max_{\eta} \sqrt{\langle \|\mathbf{u}\|^2 \rangle_z} / H$ of the responses by resolution of the equations (9) (dashed lines) and by using the approximation in (18) (solid lines).

Depending on the position of the roughness, the term $\langle \hat{h}_{1,m}(s), h_s((s-s_0)/L_s) \rangle_w$ is modified. The latter is higher when the roughness is located where the optimal roughness has a strong magnitude and a similar curvilinear periodicity. That's why the response computed with equation (18) to the roughness positioned at $s = 0.008$ has a maximum mean fluctuation rate of 2.2×10^4 against 1.6×10^3 and 3.5×10^2 for the roughness at $s_0 = 0.016$ and $s_0 = 0.056$ respectively. The perturbation triggered by the roughness located at $s_0 = 0.008$ calculated by solving the LNSE is represented in figure 7. The only

notable difference from the perturbation calculated with the approximation (18) is in the region of the roughness highlighted by the yellow ellipse, where the response exhibits a spatial structure similar to the one of the roughness. Note that a PSE method would not be able to compute the perturbation in the vicinity of the roughness since it does not capture the non-modal mechanisms triggered by the roughness (which are well reproduced when solving the LNSE (resolvent) and accounted in the resolvent analysis by the sub-optimal modes).

5.2.2. Case of a compact roughness in both the curvilinear s - and spanwise z -directions

Considering again a roughness in separate form given by equation (15), we now choose:

$$h_s(s) = \sqrt{1 - s^2} \text{ for } s \in [-1, 1] \quad \text{and} \quad h_s(s) = 0 \text{ for } |s| > 1 \quad (19)$$

$$h_z(z) = e^{-z^2}. \quad (20)$$

Hence, the roughness is a Gaussian in the z -direction localised around $z = 0$ and a semi-ellipse localised at s_0 in the s -direction with the major axis being L_s and the minor axis $He^{-z^2}/2$. We set $s_0 = 0.008 \approx 82\Delta$, $L_s/\Delta = 20.6$, $L_z/\Delta = 10.3$. The roughness shape h/H is represented in figure 9(a) and can be considered as representative, for example, of the presence of an insect on a wing surface. The spatial structure of the response calculated solving the LNSE is shown in figure 9(b). The response develops from the position of the roughness and is convected downstream in the direction of the external streamlines where it acquires the spatial structure of a cross-flow mode.

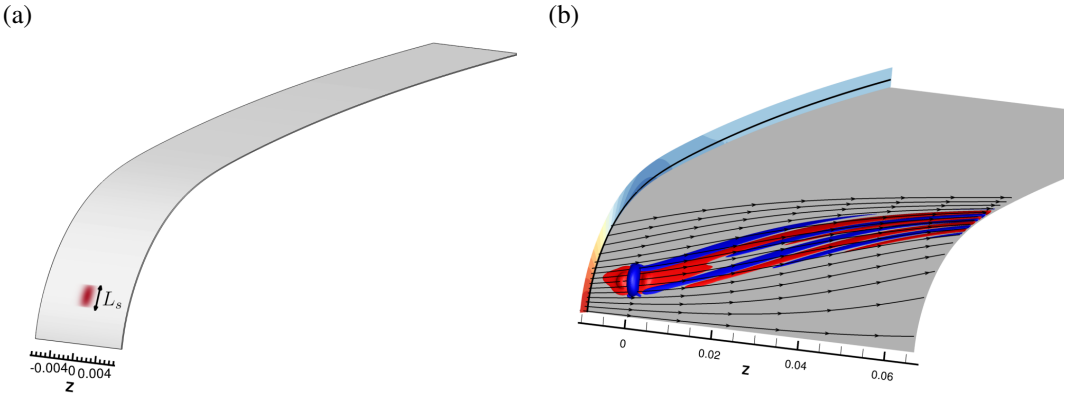


Figure 9. (a): 3D representation of the localised roughness $h(s, z)/H$ with $s_0 = 0.008 \approx 82\Delta$, $L_s/\Delta = 20.6$, $L_z/\Delta = 10.3$. (b): Spatial structure of the corresponding response calculated by solving the LNSE, with the same representation as in figure 3.

With equation (7), the wall displacement reads $h(s, z)/H = (1/2)h_s((s - s_0)/L_s) \int_{-\infty}^{+\infty} \hat{h}_{z,\beta} e^{i\beta z} d\beta$ where $\hat{h}_{z,\beta}$ is the Fourier transform of a Gaussian wave, so that $\hat{h}_{z,\beta} = (L_z/2\sqrt{\pi}) \exp(-(\beta L_z)^2/4)$. We then calculate the response of the system by using equation (12). We will, once again, make the assumption that the first singular value is sufficiently dominant to neglect the following ones. Moreover, only the roughness with spanwise wavenumber $|\beta\Delta| < 0.5$ are taken into account:

$$\frac{\mathbf{u}(x, y, z)}{H} \approx \int_0^{0.5/\Delta} \Re \left(\hat{h}_{z,\beta} \sigma_{1,\beta} \left\langle \hat{h}_{1,\beta}, h_s \left(\frac{s - s_0}{L_s} \right) \right\rangle_{\mathbf{w}} \hat{\mathbf{u}}_{1,\beta}(x, y) e^{i\beta z} \right) d\beta, \quad (21)$$

and the integral is discretised with the extended Simpson's rule with steps of $\Delta\beta = 0.001$.

In figure 10 is represented the curvilinear evolution of the wall normal maximum of the mean fluctuation rate $\max_{\eta}(\sqrt{\langle \|\mathbf{u}\|^2 \rangle_z})/H$. The response calculated from equation (21) is plotted with a

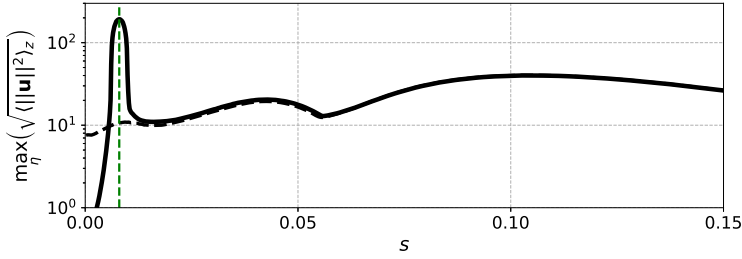


Figure 10. Curvilinear evolution of $\max_{\eta} \left(\sqrt{\langle \|\mathbf{u}\|^2 \rangle_z} \right)$ of the response computed using equation (21) (dashed line) and the exact equation (9) (solid line). The location of the centre of the roughness is shown by the green vertical dashed line.

dashed line while the response computed from the resolution of (9) is drawn with a solid line. We observe, once again, a good agreement between both responses downstream of the roughness, with a second amplification at $s = 0.054$ and two local maxima at $s = 0.042$ and $s = 0.1$ reaching respectively 19.5 and 41. As in figure 8, the fact that the maximum response magnitude is reached at the location of the roughness is related to the low energy of the response due to the strong stability of the flow configuration considered in this paper.

5.2.3. Case of chordwise and spanwise harmonic roughness

In this section, we consider a roughness of harmonic shape:

$$\frac{h(s, z)}{H} = \underbrace{\cos(\gamma s)}_{h_{\gamma}(s)} \cos(\beta z), \quad (22)$$

with $(\gamma, \beta) \in \mathbb{R}^2$. The exact and approximated responses are respectively given by:

$$\frac{\mathbf{u}(x, y, z)}{H} = \Re(\hat{\mathbf{u}}(x, y)e^{i\beta z}) \quad \text{with} \quad \hat{\mathbf{u}} = \mathbf{R}_{\beta} \mathbf{h}_{\gamma} \quad (23)$$

$$\approx \Re \left(\sigma_{\beta,1} \langle \hat{h}_{\beta,1}(s), \cos(\gamma s) \rangle_w \hat{\mathbf{u}}_{\beta,1}(x, y) e^{i\beta z} \right) = \Re \left(\pi \sigma_{\beta,1} \overline{\hat{h}_{\beta,1}(\gamma)} \hat{\mathbf{u}}_{\beta,1}(x, y) e^{i\beta z} \right), \quad (24)$$

where $\hat{h}_{\beta,j}(\gamma) = \frac{1}{\pi} \int_0^{\infty} \hat{h}_{\beta,j}(s) e^{-i\gamma s} ds$ is the Fourier transform of the j^{th} symmetric optimal roughness $\hat{h}_{\beta,j}(s)$.

In figure 11 is represented, for each couple $(\beta\Delta, \gamma\Delta) \in ([0, 0.5] \times [0, 1])$, the value of $\max_{\eta,s} \left(\sqrt{\langle \|\mathbf{u}\|^2 \rangle_z} \right) / H$ using equation (23). The same representation as figure 11 but considering equation (24) was also computed (not shown here) and gave similar results. This validates the approximation made in equation (24) and reveals that when the roughness is not localised in the curvilinear direction, the maximum amplitude of the response is well calculated by the projection on the optimal roughness, and this for all values of β and γ . Moreover, in the case of perturbations computed with the approximation (24), it is straightforward that the curvilinear position of the maximum represented in figure 11 is the same for all values of γ and corresponds to the maximum of the optimal perturbation at the value of β considered. Thus, in figure 11 are represented in black circles the curvilinear position at which the optimal perturbation reach $\max_{\eta,s} \left(\sqrt{\langle \|\hat{\mathbf{u}}_{\beta,1}\|^2 \rangle_z} \right) / H$ for each value of $\beta\Delta > 0.03$.

The spanwise wavenumbers $\beta\Delta$ associated with high values are between 0.05 and 0.25, which is directly related to the singular values σ_1 represented in figure 2. For a given spanwise wavenumber,

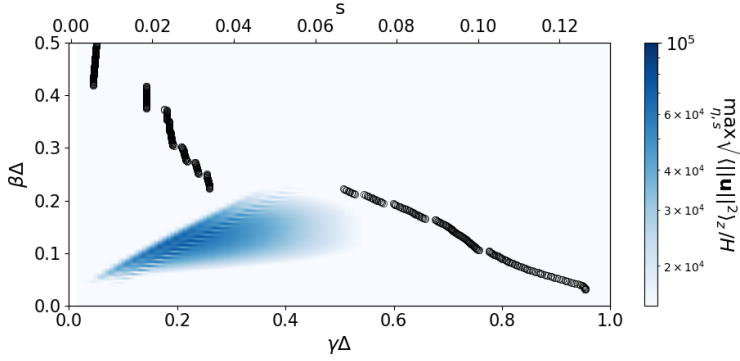


Figure 11. Representation, according to $\beta\Delta$ and $\gamma\Delta$, of $\max_{\eta,s} \left(\sqrt{\langle \|\mathbf{u}\|^2 \rangle_z} \right) / H$. The curvilinear location where the maximum of the function for optimal perturbations is reached is plotted in black circles with respect to the top axis.

the magnitude of the response is linked to the value of $|\hat{h}_{\beta,1}(\gamma)|$. For example, for $\beta\Delta = 0.11$, a first maximum is reached at $\gamma\Delta = 0.18$ even if it does not correspond to the curvilinear wavenumber of the optimal roughness at its maximum magnitude ($k_s\Delta = 0.32$ at $s = 0.008$). However, this high value is justified by the fact that, as represented in figure 5, $\gamma\Delta = 0.18$ is close to the curvilinear wavenumber of the optimal roughness over a large range of s values, including at positions where the roughness magnitude is high. Although $k_s\Delta = 0.32$ corresponds to the curvilinear wavenumber of the optimal roughness at its maximum magnitude, the strong variation of $k_s\Delta$ at $s = 0.008$ justifies the lower value of $|\hat{h}_{0.11/\Delta,1}(0.32/\Delta)|$.

As the value of β increases, the most critical γ values also increase. This is explained by the fact that, as shown in figure 6(a), the position of the magnitude maximum shifts downstream with increasing β , while remaining lower than $s = 0.016$ reached for $\beta\Delta = 0.3$. For increasing s , the direction of the external streamlines gets closer to the chordwise direction. Since the Ψ angle at the position of the maximum magnitude of the optimal roughness remains constant with increasing β (figure 6(b)), the roughness also has a direction that approaches the chordwise direction at the location of its maximum magnitude. This implies an increase of k_s at this position at least proportional to that of β , which explains the increase of the most critical γ values in figure 11. Moreover, the position of the maximum varies from $s \approx 0.005$ for $\beta\Delta = 0.5$ to $s = 0.126$ for $\beta\Delta = 0.03$. This evolution is slightly different from the one represented in figure 6 because we evaluate the maximum of different quantities. The “jumps” that can be observed between different values of $\beta\Delta$ despite the fact that the spatial structure of the optimal perturbations evolves continuously with β is related to the presence of “plateau” in the curve of $\max_{\eta} \left(\sqrt{\langle \|\hat{\mathbf{u}}_{\beta,1}\|^2 \rangle_z} \right) (s)$. The jump at $\beta\Delta = 0.22$ is linked to the switch from a position corresponding to the first amplification to a location related to the second amplification.

The overall picture indicates that the most dangerous roughness are characterised by $\beta \leq 0.5\gamma$, hence rectangular trellis elongated in the z -direction by an aspect ratio of at least 2. The characteristic size of these roughness is around $\beta\Delta \approx 0.1$, that is $L_z/\Delta \approx 60$.

These calculations can be used to make a first attempt to predict the roughness height H_c for which nonlinear effects may appear. Some studies suggest that the first nonlinear effects appear in a 3D flow when the magnitude of the disturbance velocity reaches about 10% of the baseflow velocity (Casalis & Houdeville, 2008; Tempelmann *et al.*, 2012b). Thus, considering the criterion: $\max_{\eta,s} \sqrt{\langle \|\mathbf{u}\|^2 \rangle_z} / \sqrt{2} = 0.1U^\infty$, we obtain, for a roughness with $\gamma\Delta = 0.18$, a critical height value of $H_c = 4.92 \times 10^{-6} \approx 4.9\%c\Delta$ for $\beta\Delta = 0.11$. It corresponds to the order of magnitude of the wall defects that can be encountered on real wings (Radeztsky & Saric, 1999). This is therefore a first indication that we could see non-linear

effects appear before the end of the domain in these flow conditions for unpolished aerofoils. For a roughness of height $H = 4.92 \times 10^{-6}$, the criterion is reached for $s = 0.1$. It is important to note that this roughness size is small enough to allow the linearisation of the wall boundary condition to remain valid. Indeed, in our case, the displacement thickness δ^* is greater than 10^{-4} and the approximation remains valid for roughness of height below $5\% \delta^*$ (Schrader & Henningson, 2009; Tempelmann *et al.*, 2012b).

6. Conclusion

In this paper, we studied the receptivity of a swept aerofoil to wall roughness using wall displacement based resolvent analysis. An incompressible flow covering the whole leading edge was considered using a global framework. We have identified the most critical spanwise and curvilinear wavenumbers, as well as the spatial structure of the optimal roughness and associated perturbations. In the case of the spanwise wavenumber with the highest dominant singular value, the optimal response corresponds to a cross-flow mode with two local maxima. The optimal roughness is located near the attachment-line with a wavevector nearly orthogonal to the external streamlines. Moreover, the increase of the spanwise wavenumber shifts the location of the optimal roughness further downstream and the location of the optimal response closer to the attachment-line. The most amplified curvilinear wavenumbers rise with increasing spanwise wavenumber. For all spanwise wavenumbers, the optimal roughness has a maximum magnitude close to the attachment-line, confirming the results of previous studies (Tempelmann *et al.*, 2012a; Radeztsky & Saric, 1999; Thomas & Ashworth, 2017). When the resolvent operator is low-rank (few dominant singular values dominate), the optimal roughness and associated responses provide a low-order model. Once the optimal roughness and perturbations have been computed, the low-order model can be used to compute the flow response to any small amplitude roughness shape at a reduced computational cost compared to the direct resolution of the LNSE.

Responses to various roughness (periodic and compact in both chordwise and spanwise directions) were finally computed. We verified that the magnitude of the response is the highest when the roughness has a Fourier transform involving spanwise wavenumbers corresponding to the highest singular values and curvilinear wavenumbers representative of the optimal roughness over a large range of s where its amplitude is high. Approximate responses calculated with a single singular value were compared to the responses obtained from the resolution of the LNSE and showed good agreement downstream of the roughness. When the roughness is localised in the curvilinear direction, a peak of magnitude can appear at the location of the roughness that cannot be captured by the low-rank method. In particular, this shows that the knowledge of the spatial structure of some optimal perturbations allows us to predict the characteristics of the response to a wide range of roughness. A first attempt to predict the height of a non-localised square wave roughness required to trigger nonlinear effects before $X = 15\%$ was made. A critical roughness height around 10^{-6} was found for a square wave roughness with a spanwise wavenumber matching the one of the most amplified optimal roughness. This size being of the order of the wall defect sizes that can be found on realistic aerofoils, it is a first indication of the possible transition before $X = 15\%$ in this particular flow conditions. One possible prospect of this work is to compare the results of the resolvent analysis with experimental or DNS results.

Acknowledgment

The authors thank Jean-Philippe Brazier for providing the local stability analysis code.

Funding Statement. The study was supported by a grant from the Agence de l'innovation de défense (Defence Innovation Agency).

Declaration of Interests. The authors declare no conflict of interest.

Data Availability Statement. Further details on underlying data are available from the corresponding author (E.K.).

Ethical Standards. The research meets all ethical guidelines, including adherence to the legal requirements of the study country.

References

- AHMED, NAVEED & RUBINO, SAMUELE 2019 Numerical comparisons of finite element stabilized methods for a 2d vortex dynamics simulation at high reynolds number. *Computer Methods in Applied Mechanics and Engineering* **349**, 191–212.
- AMESTOY, P.R., BUTTARI, A., L'EXCELLENT, J.-Y. & MARY, T. 2019 Performance and Scalability of the Block Low-Rank Multifrontal Factorization on Multicore Architectures. *ACM Transactions on Mathematical Software* **45**, 2:1–2:26.
- AMESTOY, P.R., DUFF, I. S., KOSTER, J. & L'EXCELLENT, J.-Y. 2001 A fully asynchronous multifrontal solver using distributed dynamic scheduling. *SIAM Journal on Matrix Analysis and Applications* **23** (1), 15–41.
- ARNAL, D. & CASALIS, G. 2000 Laminar-turbulent transition prediction in three-dimensional flows. *Progress in Aerospace Sciences* **36** (2), 173–191.
- BALAY, SATISH, ABHYANKAR, SHRIRANG, ADAMS, MARK F., BENSON, STEVEN, BROWN, JED, BRUNE, PETER, BUSCHELMAN, KRIS, CONSTANTINESCU, EMIL, DALCIN, LISANDRO, DENER, ALP, EIJKHOUT, VICTOR, FAIBUSSOWITSCH, JACOB, GROPP, WILLIAM D., HAPLA, VÁCLAV, ISAAC, TOBIN, JOLIVET, PIERRE, KARPEEV, DMITRY, KAUSHIK, DINESH, KNEPLEY, MATTHEW G., KONG, FANDE, KRUGER, SCOTT, MAY, DAVE A., MCINNES, LOIS CURFMAN, MILLS, RICHARD TRAN, MITCHELL, LAWRENCE, MUNSON, TODD, ROMAN, JOSE E., RUPP, KARL, SANAN, PATRICK, SARICH, JASON, SMITH, BARRY F., ZAMPINI, STEFANO, ZHANG, HONG, ZHANG, HONG & ZHANG, JUNCHAO 2022 PETSc/TAO users manual. *Tech. Rep.* ANL-21/39 - Revision 3.18. Argonne National Laboratory.
- CARPENTER, A. SARIC, W. & REED, H. 2008 Laminar flow control on a swept wing with distributed roughness.
- CASALIS, D. ARNAL, G. & HOUEVILLE, R. 2008 Practical transition prediction methods: subsonic and transonic flows. *VKI Lectures Series Advances in Laminar-Turbulent Transition Modelling*.
- CHOUDHARI, MEELAN 1994 Roughness-induced generation of crossflow vortices in three-dimensional boundary layers. *Theoretical and Computational Fluid Dynamics* **6** (1), 1–30.
- COLLIS, S. & LELE, S. 1999 Receptivity to surface roughness near a swept leading edge. *Journal of Fluid Mechanics* **380**, 141–168.
- CORBETT, PETER & BOTTARO, ALESSANDRO 2001 Optimal linear growth in swept boundary layers. *Journal of Fluid Mechanics* **435**, 1–23.
- CROUCH, J. 1993 Receptivity of three-dimensional boundary layers. In *31st Aerospace Sciences Meeting*, p. 74.
- DEYHLE, H. & BIPPES, H. 1996 Disturbance growth in an unstable three-dimensional boundary layer and its dependence on environmental conditions. *Journal of Fluid Mechanics* **316**, 73–113.
- HECHT, F. 2012 New development in freefem++. *Journal of Numerical Mathematics* **20** (3-4), 1–14.
- HERBERT, T. 1988 Secondary instability of boundary layers. *Annual review of fluid mechanics* **20** (1), 487–526.
- HERNANDEZ, J. ROMAN, V. & VIDAL, V. 2005 SLEPC: A scalable and flexible toolkit for the solution of eigenvalue problems. *ACM Trans. Math. Software* **31** (3), 351–362.
- HOUEVILLE, R. 1992 Three-dimensional boundary layer calculation by a characteristic method. In *Fifth Symposium on Numerical and Physical Aspects of Aerodynamic Flows, Long Beach, January 1992*.
- KITZINGER, EURYALE, LECLERCQ, TRISTAN, MARQUET, OLIVIER, PIOT, ESTELLE & SIPP, DENIS 2023 Attachment-line, cross-flow and tollmien–schlichting instabilities on swept onera-d and joukowski airfoils. *Journal of Fluid Mechanics* **957**, A29.
- MACK, C. & SCHMID, P. 2011 Global stability of swept flow around a parabolic body: The neutral curve. *Journal of Fluid Mechanics* **678**.
- MOULIN, JOHANN, JOLIVET, PIERRE & MARQUET, OLIVIER 2019 Augmented lagrangian preconditioner for large-scale hydrodynamic stability analysis. *Computer Methods in Applied Mechanics and Engineering* **351**, 718–743.
- MÜLLER, B. & BIPPES, H. 1989 Experimental study of instability modes in a three-dimensional boundary layer. In *AGARD*.
- PRESS, WILLIAM H, TEUKOLSKY, SAUL A, VETTERLING, WILLIAM T & FLANNERY, BRIAN P 2007 *Numerical recipes 3rd edition: The art of scientific computing*. Cambridge university press.
- RADEZTSKY, M. REIBERT, R. & SARIC, W. 1999 Effect of isolated micron-sized roughness on transition in swept-wing flows. *AIAA Journal* **37**, 1370–1377.
- REED, H. & SARIC, W. 1989 Stability of three-dimensional boundary layers. *Annual Review of Fluid Mechanics* **21** (1), 235–284.
- REED, H., SARIC, W. & ARNAL, D. 1996 Linear stability theory applied to boundary layers. *Annual review of fluid mechanics* **28** (1), 389–428.
- SARIC, H. REED, W. & WHITE, E. 2003 Stability and transition of three-dimensional boundary layers. *Annual Review of Fluid Mechanics* **35**, 413–440.

- SCHMID, P. & HENNINGSON, D. 2001 *Stability and Transition in Shear Flows*, , vol. 142.
- SCHRADER, L. BRANDT, L. & HENNINGSON, D. 2009 Receptivity mechanisms in three-dimensional boundary-layer flows. *Journal of Fluid Mechanics* **618**, 209–241.
- SIPP, DENIS & MARQUET, OLIVIER 2013 Characterization of noise amplifiers with global singular modes: the case of the leading-edge flat-plate boundary layer. *Theoretical and Computational Fluid Dynamics* **27** (5), 617–635.
- SYMON, S. ROSENBERG, S. & MCKEON, B. 2018 Non-normality and classification of amplification mechanisms in stability and resolvent analysis. *Physical Review Fluids* **3** (5), 053902.
- TEMPELMANN, DAVID, HANIFI, ARDESHIR & HENNINGSON, DAN S 2010 Spatial optimal growth in three-dimensional boundary layers. *Journal of Fluid Mechanics* **646**, 5–37.
- TEMPELMANN, DAVID, HANIFI, ARDESHIR & HENNINGSON, DAN S 2012a Swept-wing boundary-layer receptivity. *Journal of Fluid Mechanics* **700**, 490–501.
- TEMPELMANN, DAVID, SCHRADER, LARS-UVE, HANIFI, ARDESHIR, BRANDT, LUCA & HENNINGSON, DAN S 2012b Swept wing boundary-layer receptivity to localized surface roughness. *Journal of Fluid Mechanics* **711**, 516–544.
- THOMAS, S. MUGHAL, C. & ASHWORTH, R. 2017 On predicting receptivity to surface roughness in a compressible infinite swept wing boundary layer. *Physics of Fluids* **29** (3), 034102.
- TOWNE, AARON, RIGAS, GEORGIOS & COLONIUS, TIM 2019 A critical assessment of the parabolized stability equations. *Theoretical and Computational Fluid Dynamics* **33**, 359–382.
- TREFETHEN, L. TREFETHEN, S. & DRISCOLL, T. 1993 Hydrodynamic stability without eigenvalues. *Science* **261** (5121), 578–584.
- WASSERMANN, PETER & KLOKER, MARKUS 2005 Transition mechanisms in a three-dimensional boundary-layer flow with pressure-gradient changeover. *Journal of Fluid Mechanics* **530**, 265–293.